

**Scientific and Technological Alliance for
Guaranteeing the European Excellence in
Concentrating Solar Thermal Energy**



FP7 Grant Agreement number: 609837
Start date of project: 01/02/2014
Duration of project: 48 months

STAGE-STE milestone 35

**MS 35: Intermediate status of
thermochemical energy storage assessed**

WP9 – Tasks 9.2	Milestone 35 (MS35)
Reached/Submitted:	July 2016
Work Package Leader:	PSI
Task leader:	PSI
Author(s):	Laurie André (CNRS), José Gonzalez (IMDEA), Manuel Romero (IMDEA), Stefan Ströhle (PSI)
Revised by:	Stéphane Abanades (CNRS)
Document version:	3
Reviewed/supervised by:	Gilles Flamant (CNRS), Anton Meier (PSI)

Table of contents

1. INTRODUCTION.....	3
2. SELECTION OF SUITABLE THERMOCHEMICAL SYSTEMS (CNRS).....	4
3. METAL OXIDES REDOX REACTIONS.....	5
3.1. COBALT OXIDE (CNRS)	5
3.2. MANGANESE OXIDE (CNRS AND IMDEA).....	7
3.3. MANGANESE-CERIA OXIDE (IMDEA)	13
3.4. PEROVSKITES (CNRS).....	13
4. INTEGRATION OF THERMOCHEMICAL STORAGE SYSTEMS: A CASE STUDY (PSI)	15
5. LIST OF ABBREVIATIONS.....	21
6. REFERENCES	22

1. Introduction

In the frame of STAGE-STE, potential thermochemical energy storage systems are studied in order to develop alternatives to sensible and latent thermal energy storage systems. The study first began by a literature survey coupled with an analysis of thermodynamic chemical equilibrium, which served as a primary selection of potential candidates for thermochemical energy storage. Among the candidate systems, metal oxides are convenient to work with air in an open loop since the reacting gas is O_2 . Redox reactions based on metal oxides were studied at oxygen partial pressure $P_{O_2} = 0.2$ atm in order to mimic air atmosphere. The improvement of redox performances for manganese oxide and cobalt oxide was investigated through the synthesis of mixed metal oxides (addition of Fe). The perovskite structure is also interesting for enhanced oxygen exchange capacity, thus the redox behaviour and the reaction reversibility of several Ba and Sr-based formulations were studied for thermochemical energy storage application.

2. Selection of suitable thermochemical systems (CNRS)

The selection of interesting thermochemical energy storage candidates is done regarding their compatibility with CSP plants and suitability with a set of criteria [1]-[3], such as high reaction temperature (400-1200°C), complete reaction reversibility, high reaction enthalpy, fast reaction kinetics, cycling stability, high availability, low cost, and non-toxicity of materials.

The theoretical transition temperatures and the energy storage capacity of selected metal oxide candidates are listed in Table 1.

Table 1 Theoretical transition temperature and energy storage capacity of selected metal compounds in 20% of reacting gas.

Chemicals	Transition temperature (°C)	Gravimetric energy density (kJ/kg)
BaO ₂ /BaO	775	432.6
Co ₃ O ₄ /Co ₂ O ₃	790	816.1
Mn ₂ O ₃ /Mn ₃ O ₄	820	190.1
CuO/Cu ₂ O	1025	810.2
Fe ₂ O ₃ /Fe ₃ O ₄	1290	485.6
Mn ₃ O ₄ /MnO	1575	850.6

Experiments showed that Co₃O₄ is the most suited raw material given the fast reaction kinetics and complete reaction reversibility. However, the cost and potential toxicity of cobalt oxide requires the enhancement of other alternative materials. Optimization of materials reactivity is required for the other metal oxide species by using e.g. doping strategies, controlled synthesis techniques for tailored morphology, stabilization with inert materials to alleviate sintering effects, etc. The reaction kinetics and the thermodynamic properties of the selected materials need to be characterised, as well as their performance stability over successive cycles, in order to confirm the suitability of the chosen materials for thermal energy storage (TES) application. Then, the design and testing of adapted solar reactor concepts will also be required to demonstrate the feasibility of materials processing in solar reactor prototypes during solar heat charging and discharging. Furthermore, raw materials were mostly addressed so far, but recent research concerning the efficiency of hybrid materials, such as mixed metal oxides and perovskites, is promising and these materials need to be explored.

3. Metal oxides redox reactions

Various metal oxides have been studied for thermochemical heat storage applications [4] due to their high gravimetric storage density, which is important for lowering the necessary amount of reactant involved in large-scale processes. The two-step thermochemical redox reactions considered for metal oxides are as follows:



Because the amount of reacting gas greatly affects the transition temperatures of the materials, metal oxides were tested in a reduction and oxidation atmosphere of 20% O₂-Ar in order to observe the feasibility of a thermochemical energy storage system using air.

3.1. Cobalt oxide (CNRS)

Most research focusing on metal oxides is considering cobalt oxide as promising thermochemical energy storage material. The reduction temperature of CO₃O₄ to CoO in air atmosphere is estimated to be between 880 and 930°C according to the literature [5]-[8]. Cobalt oxide was tested as heat storage material in the form of powder [5], foam [6]-[7] and pellets [8]. While Karagiannakis *et al.* (2014) [8] obtained the highest measured energy density of 515 kJ/kg for the pellet and state that the structured material exhibits better heat transfer than powder, Agrafiotis *et al.* (2015) [6]-[7] noticed the presence of cracks appearing in pellets after a few cycles while foams showed better mechanical stability. The addition of a secondary metal oxide can be a way to modify the properties of a pure oxide. The cyclability and transition temperature of cobalt oxide was tested after the addition of various secondary oxides, and Block *et al.* (2014) [9] reported that both addition of iron oxide to cobalt oxide or addition of cobalt oxide to iron oxide reduces the enthalpies of reaction compared to those of the pure oxides. However, they estimated that 10% iron oxide doped cobalt oxide is still showing high enthalpy of reaction and possesses higher reduction/oxidation reversibility than pure cobalt oxide. This phenomenon is being investigated here by the synthesis and analysis of mixed Co-Fe oxide systems (Figure 1 and Figure 2). For this study, CNRS used thermogravimetric analysis (TGA) to investigate the redox properties and reaction reversibility of the thermochemical systems.

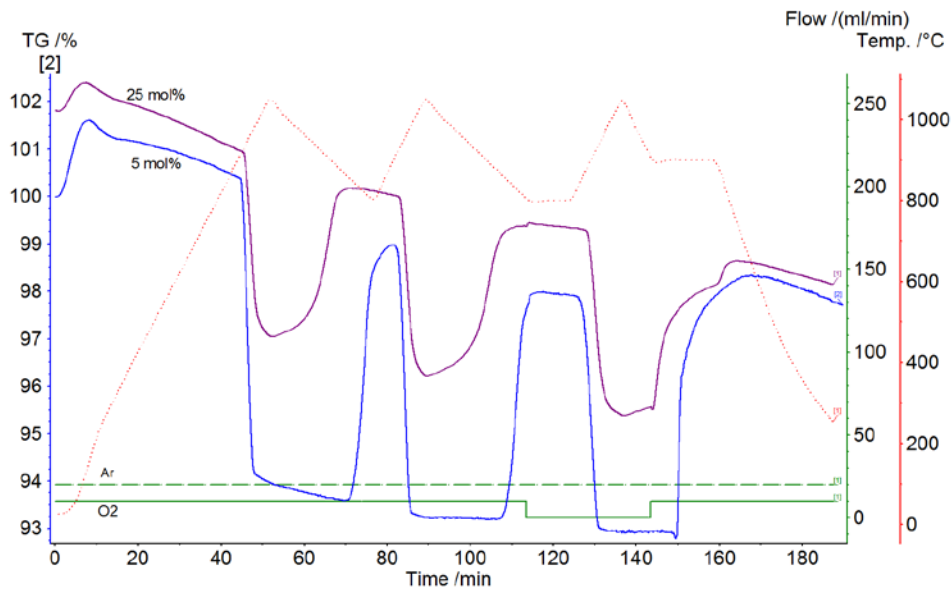


Figure 1 TGA of cobalt oxide synthesized by Pechini method with 25 mol% Fe and 5 mol% Fe, respectively.

An effect of Fe addition on the temperatures of reduction and oxidation is also visible. As both temperatures rise with more Fe addition, it can be noticed that at 25 mol% of added Fe the gap between the reduction and oxidation temperatures has been reduced (Figure 2). The reduction of this gap in temperature is interesting for large-scale application since it reduces the amount of energy spent for the heating and cooling of the system.

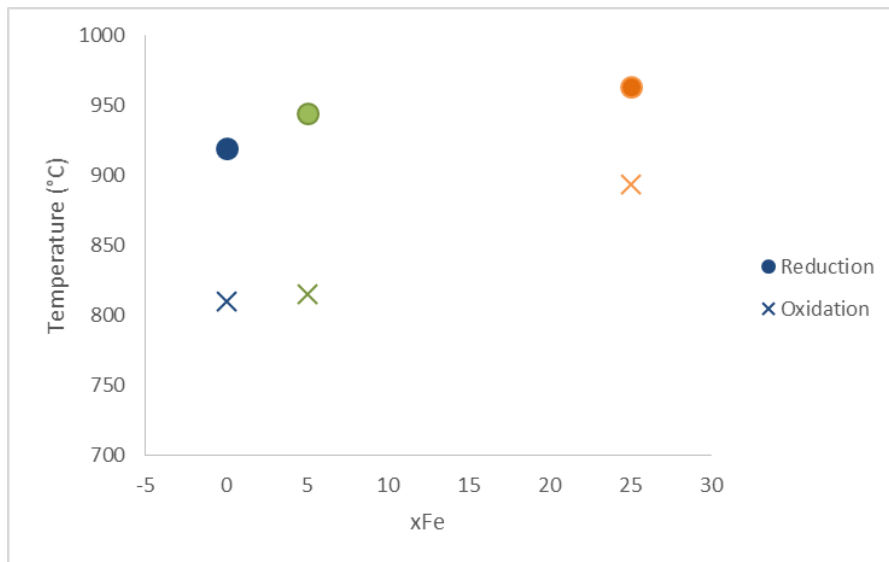


Figure 2 Reduction and oxidation temperatures at peak reaction rate for pure cobalt oxide and with the addition of 5 mol% and 25 mol% of iron oxide.

3.2. Manganese oxide (CNRS and IMDEA)

Manganese compounds are excellent candidates as heat storage material due to their outstanding characteristics (low cost, environmentally friendly, reaction temperature, etc.). The Mn-O system is rather complex with various stable crystalline phases (MnO_2 , Mn_2O_3 , Mn_3O_4 and MnO) depending on the temperature and oxygen partial pressure.

CNRS contribution

Concerning the $\text{Mn}_2\text{O}_3/\text{Mn}_3\text{O}_4$ couple, the reduction step of manganese oxide was observed in the range of 920-1000°C and the notably slow re-oxidation was observed in the range of 850-500°C with a gravimetric energy storage density of 110 kJ/kg. It is specified that the re-oxidation happens in two steps, the first one being during the cooling and in between 700°C-500°C, and the second one being during the re-heating and in the range of 500-850°C [8]. As $\text{Mn}_2\text{O}_3/\text{Mn}_3\text{O}_4$ is a promising metal oxide redox pair for thermochemical heat storage, Carillo *et al.* (2014) [10] tested the durability of this material over thirty oxidation-reduction cycles performed by thermogravimetry. They enlightened the necessity to pay attention to the initial particle size of these oxides since it influences the kinetics and the thermodynamics of the reaction. Especially, smaller particles would contribute in lowering the oxidation temperature, but it would also hinder the diffusion of O_2 by favouring the sintering of the material. Based on these results, the influence of the morphology of the material on its reactivity is currently under investigation by considering different synthesis techniques (Figure 3).

Carillo *et al.* (2015) [11] further studied the performances of manganese oxide for thermochemical energy storage and sought to improve it with the addition of iron oxide to the material. The incorporation of iron oxide does not allow avoiding the sintering encountered with manganese oxide, however it increases the heat storage density of the material and it stabilizes and enhances its oxidation rate over an experiment of thirty redox cycles. The material presenting the fastest and the most stable oxidation reactions in their study is Mn_2O_3 doped with 20% Fe. Carillo *et al.* (2015) [12] also considered Fe-Cu co-doping in manganese oxide in order to study its effect on the temperature gap of about 200°C between the reduction and oxidation temperatures of this material, as well as the effects on its reaction kinetics. They showed the possibility to reduce the reduction temperature with the incorporation of Cu and to increase the oxidation temperature with the incorporation of Fe. However, they also reported lower reduction and oxidation rates with the addition of 5% Cu. In the study by CNRS, the improvement of the reactivity of manganese oxide through the addition of iron oxide was investigated. It was observed that the addition of iron had an effect on the reactivity of the material as well as on its reduction and oxidation temperatures (Figure 4).

The addition of higher amounts of Fe in Mn_2O_3 increases the temperatures of reaction but also decreases the gap in temperature between the reduction and the oxidation step.

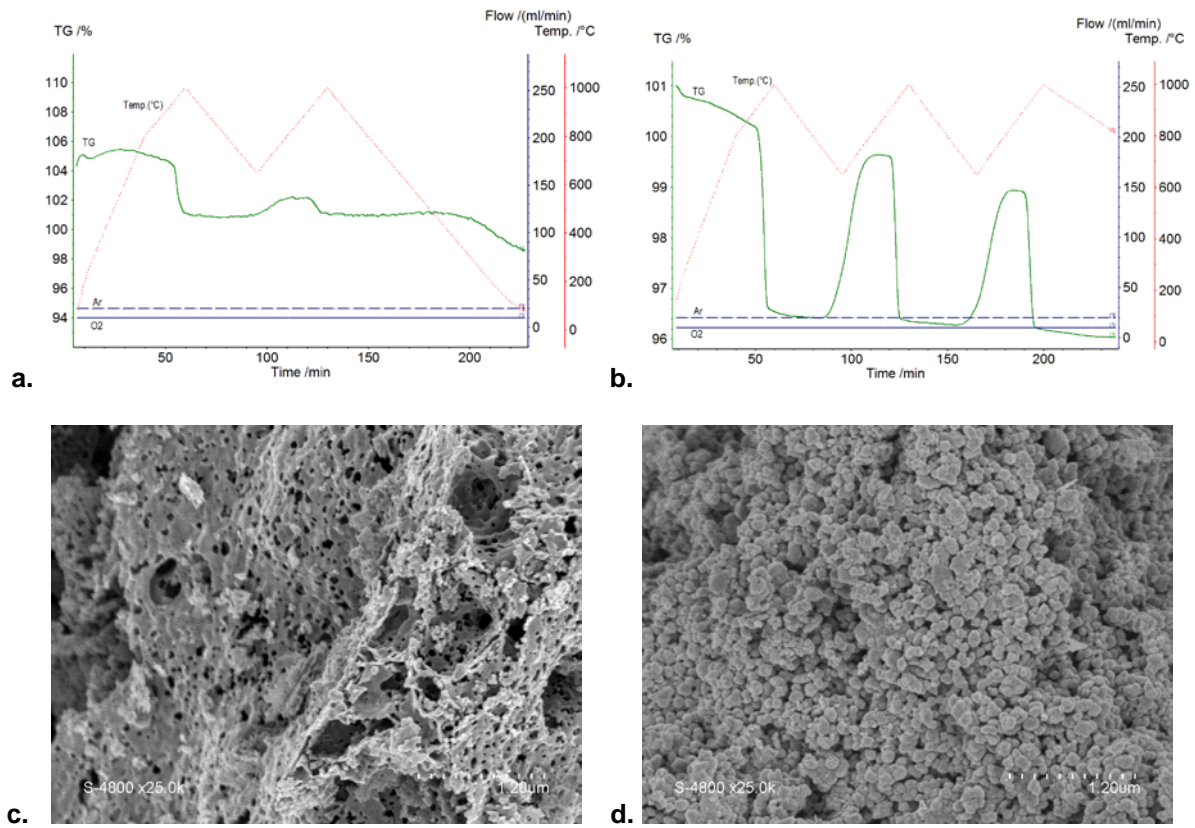


Figure 3 TGA of (a) porous Mn₂O₃ and (b) nanometre sized particles Mn₂O₃; SEM of (c) porous Mn₂O₃ and (d) nanometre sized particles Mn₂O₃.

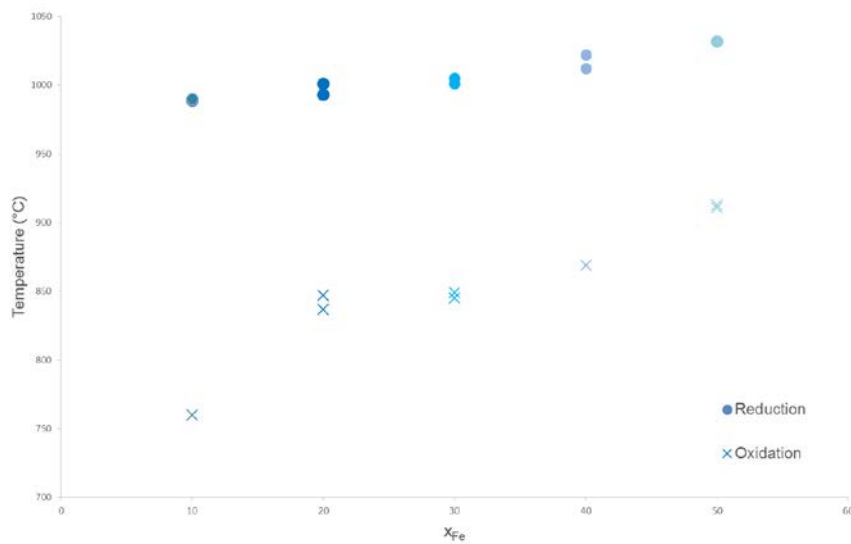


Figure 4 Peak reaction rate temperatures of Mn₂O₃ mixed with 10, 20, 30, 40 and 50 mol% Fe, respectively.

IMDEA contribution

Current analysis addresses the following reversible redox chemical reaction:



Figure 5 shows typical thermogravimetric behaviour of Mn_3O_4 (Manganese Oxide Mn_3O_4 -LH from Erachem Comilog SA was selected for this activity). Below 350°C , there is a small weight decrease associated to the loss of some volatiles, free water and some of the combined water (OH^- groups). Between 350°C and 650°C , the sample weight increases in two consecutive steps corresponding to the oxidation of the different Mn oxides co-existing in the sample until achieving the complete conversion to Mn_2O_3 . Thermal reduction to Mn_3O_4 proceeds at around 950°C .

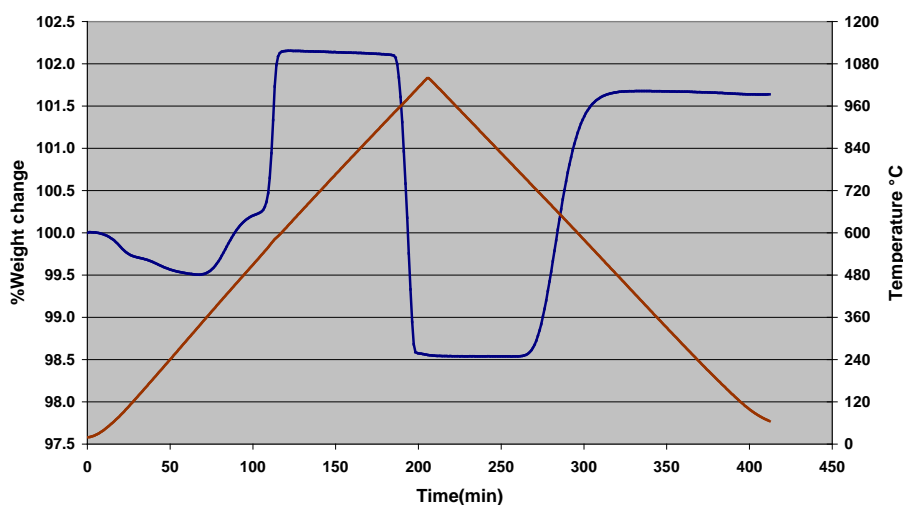


Figure 5 Typical TGA of a oxidation/reduction/oxidation cycle of Mn_3O_4 under air flow 75ml/min.

Chemical, physical and structural analysis

Chemical analysis of Mn_3O_4 -LH powders was obtained using a Perkin Elmer ICP-OES Spectrometer. It shows that the material contains 73.6% of Mn with an oxidation state of 2.7. Other minor chemical elements are presented in the material such as Ni, K, Na, Mg, Ca, Ba, Sr, Fe, Si, etc. Physical properties were measured by nitrogen adsorption-desorption isotherm with a Quantachrome QuadraSorb-S analyser. Mn_3O_4 -LH powders present a total pore volume of $0.040 \text{ cm}^3/\text{g}$ and a specific surface area of $13.0 \text{ m}^2/\text{g}$. The structural analysis was performed by X-Ray Diffraction (XRD) using a Bruker XRD diffractometer, as shown in Figure 6.

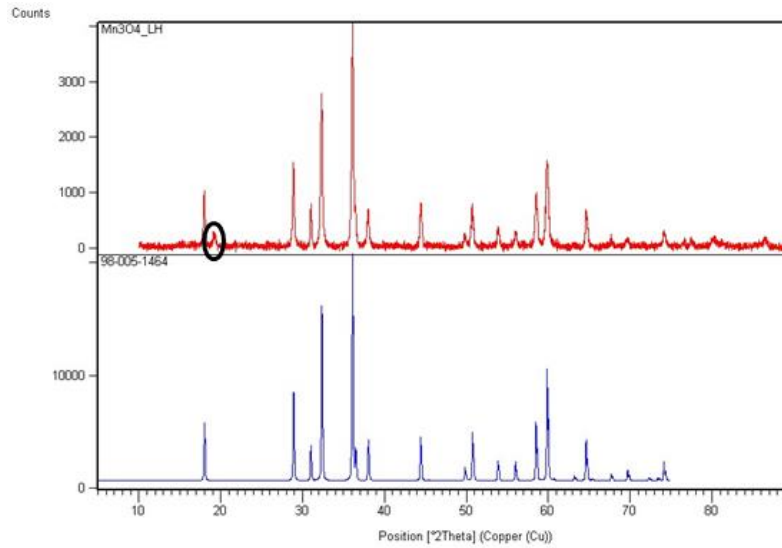


Figure 6 XRD diffractogram of Mn_3O_4 -LH.

XRD peaks observed for Mn_3O_4 -LH agree with diffraction patterns of Mn_3O_4 hausmannite (JCPDS- 98-005-1464), except for a diffraction peak at 19.2° that is associated to impurities of Mn_3O_4 -LH powders. According to the ‘Scherrer’ estimation, Mn_3O_4 -LH powders show a crystallite size around 40 nm, which well corresponds to the ‘average’ of primary crystals observed by scanning electron microscopy (SEM) and high-resolution scanning electron microscopy (HRSEM) (see Figure 7).

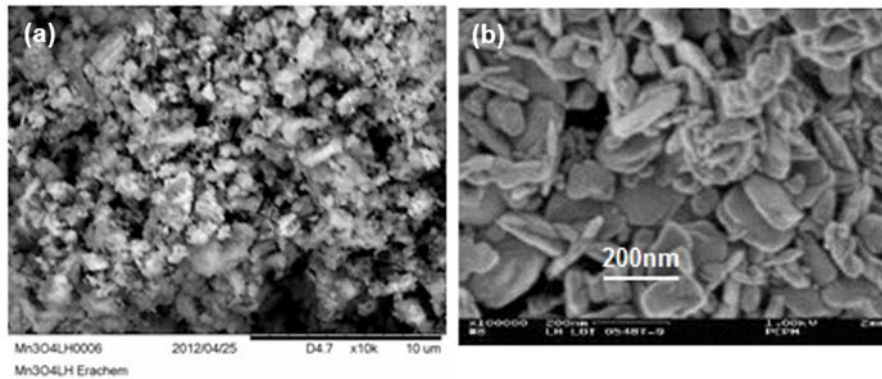


Figure 7 Micrographs of SEM (a) and HRSEM (b) of Mn_3O_4 -LH.

Thermochemical behaviour of Mn_3O_4

Thermogravimetric analyses (TGA) studies were performed using a SDT Q-600 from TA Instruments using a temperature program between 1000°C to 550°C with a rate of 10°C/min in 100 ml/min air flow. Figure 8 (left) shows the thermogravimetric plot obtained for the 50 cycles of heating and cooling between 550 to 1000 °C. It can be observed that Mn_3O_4 -LH maintains its good cyclability along the experiment. Figure 8 (right) presents a zoom on the first three heating/cooling cycles of Mn_3O_4 -LH and the analysis shows an unusual behaviour during the first cycle. This behaviour is associated to impurities of Mn_3O_4 -LH powders, agreeing with previous results of XRD. Mn_3O_4 -LH powders were then subjected to a thermal treatment (Table 2) in order to eliminate the impurities in the powder.

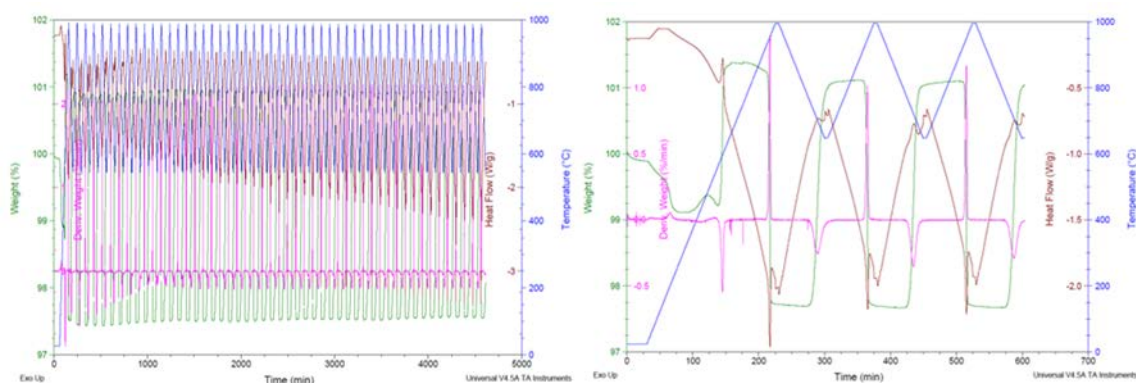


Figure 8 First cycle and 50 cycles of heating and cooling obtained for Mn_3O_4 -LH.

Table 2 Thermal treatments parameters applied to Mn_3O_4 -LH.

Temperature	Period	Atmosphere
between 600 to 1000 °C	between 30 minutes to 4 hours	Air or Argon

The effect caused by the corresponding thermal treatment was measured by structural analysis and thermal characterization. Figure 9 shows the high temperature XRD results of Mn_3O_4 -LH in air. Two different crystalline structure modifications were observed depending on the temperature. The first one takes place during the heating between 576 to 640°C, associated to the change in structure from Mn_3O_4 (hausmannite) to Mn_2O_3 (bixbyite). The second change occurs during the cooling and is associated to the re-transformation from Mn_2O_3 (bixbyite) to Mn_3O_4 (hausmannite).

At higher temperatures, XRD analysis in argon only shows a single crystalline phase up to 800°C associated to Mn_3O_4 . This behaviour is due to the absence of oxygen that prevents the oxidation of Mn_3O_4 to Mn_2O_3 .

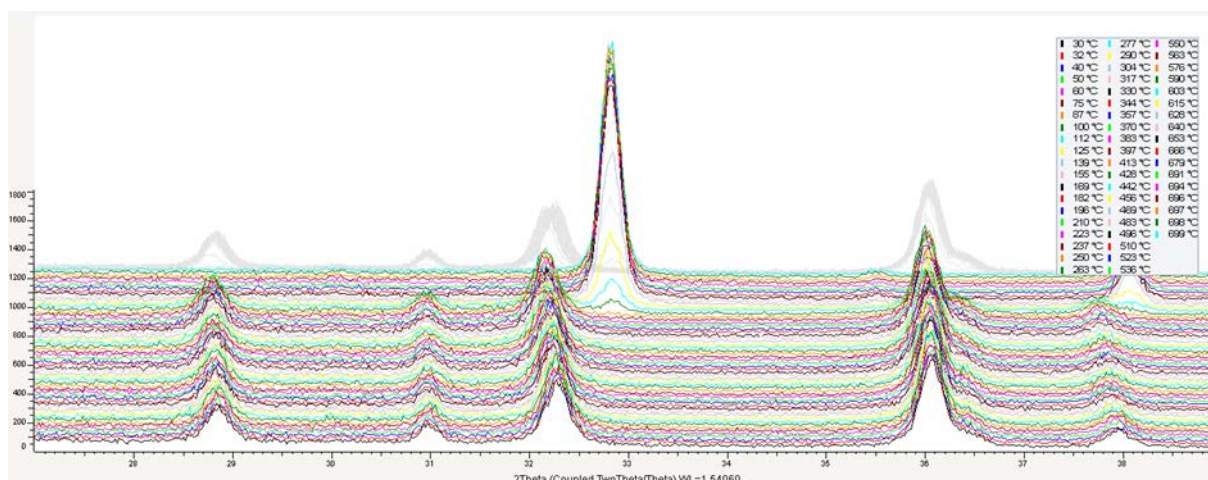


Figure 9 High temperature XRD measurements of Mn₃O₄-LH in argon.

Crystal size of Mn₃O₄-LH with different thermal treatments was estimated using Scherrer's estimation (Figure 10, left). Figure indicates that the thermal treatment produces an increment of the crystal size of Mn₃O₄-LH, which becomes more important when the temperature increases.

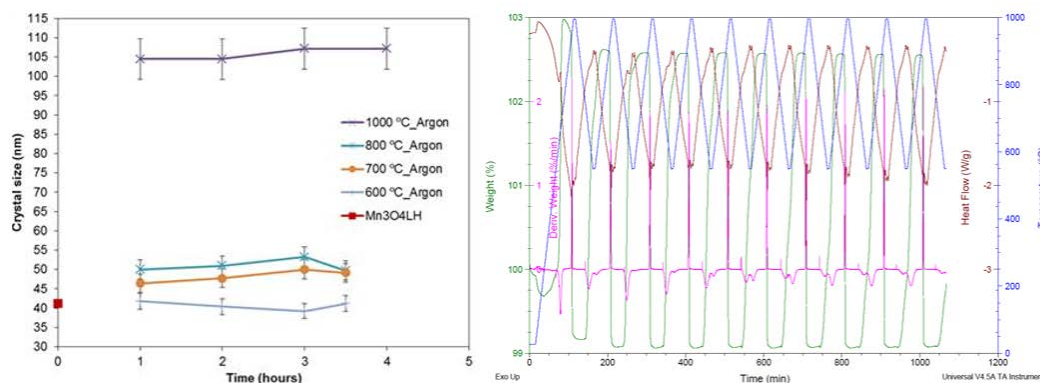


Figure 10 Crystal size of Mn₃O₄-LH powders with different thermal treatments in argon (left); Cyclability test of Mn₃O₄-LH treated for 1 hour at 600°C in air (right).

Thermogravimetric analyses of Mn₃O₄-LH points out that the thermochemical behaviour can be affected notably when performing the thermal treatment at temperatures higher than 600°C and residence times in the oven longer than 1 hour. Figure 10 (right) shows the TGA of Mn₃O₄-LH treated at 550°C during 30 minutes. After ten cycles, initial thermochemical properties Mn₃O₄-LH were maintained during the experiment compared to Mn₃O₄-LH without treatment.

3.3. Manganese-ceria oxide (IMDEA)

A potential way to improve the material performance in terms of cyclability and/or working temperature of thermochemical materials is by mixing metal oxides of different melting points. This route could allow for stabilizing the overall particle structure avoiding sintering and enhancing the kinetics if one of the oxides acts as oxygen donor centre. Mn_3O_4 and CeO_2 have been retained for analysing this concept.

The mixtures have been prepared by mechanical milling using a ball mixer PM 100 CM Retsch. Different parameters are under study, such as Mn/Ce molar ratio, solvent molar ratio, milling time, spin rate (rpm), and thermal treatment.

First experimental results show the big effect of the manganese oxide content on the cyclability of the mixture $\text{Mn}_3\text{O}_4/\text{CeO}_2$; samples with a higher molar ratio of Mn_3O_4 showed better thermochemical performance. Thus, the molar ratio of the mixture contents could be a key parameter to define the cyclability of the final material.

Further experimental activities will focus on optimizing the synthesis and characterizing $\text{Mn}_3\text{O}_4/\text{CeO}_2$ mixtures depending on their chemical, physical and thermochemical properties.

3.4. Perovskites (CNRS)

ABO_3 structured perovskites present a high oxygen mobility and the ability to release and incorporate oxygen during cyclic endothermic reduction and exothermic oxidation. Further work on perovskites may lead to potential application to TES [13]. Sr and Ba-based perovskites were studied as oxygen sorbents [14]-[19]. $\text{La}_x\text{Sr}_{1-x}\text{Co}_y\text{Mn}_{1-y}\text{O}_{3-\delta}$ (LSCM) and $\text{La}_x\text{Sr}_{1-x}\text{Co}_y\text{Fe}_{1-y}\text{O}_{3-\delta}$ were presented by Babiniec *et al.* (2015) [16] for their good reduction/oxidation reactivity. In the study by CNRS, the objective was to assess the potential of Ba and/or Sr perovskites in solar thermochemical processes for energy storage application. The study aimed to identify the materials that exhibit the largest amounts of oxygen that can be released over the course of the reduction steps, and that at the same time can re-incorporate the same amount of oxygen in a complete reversible way. The reversibility of reduction and oxidation reactions was investigated to screen the most attractive materials. The studied perovskite-based materials with different compositions considered were $\text{SrMnO}_{3-\delta}$, $\text{SrCoO}_{3-\delta}$, $\text{SrFeO}_{3-\delta}$, $\text{BaCoO}_{3-\delta}$, $\text{BaFeO}_{3-\delta}$, $\text{BaMnO}_{3-\delta}$, $\text{SrCo}_{0.8}\text{Fe}_{0.2}\text{O}_{3-\delta}$, $\text{SrCo}_{0.2}\text{Fe}_{0.8}\text{O}_{3-\delta}$, $\text{Ba}_{0.5}\text{Sr}_{0.5}\text{CoO}_{3-\delta}$, $\text{Ba}_{0.5}\text{Sr}_{0.5}\text{FeO}_{3-\delta}$, $\text{Ba}_{0.5}\text{Sr}_{0.5}\text{Co}_{0.8}\text{Fe}_{0.2}\text{O}_{3-\delta}$ and $\text{Ba}_{0.5}\text{Sr}_{0.5}\text{Co}_{0.2}\text{Fe}_{0.8}\text{O}_{3-\delta}$ [20]. The heating steps and operating conditions used for TGA experiments are presented in Figure 11. The corresponding thermochemical redox cycle behaviour of Sr-based perovskites is also shown.

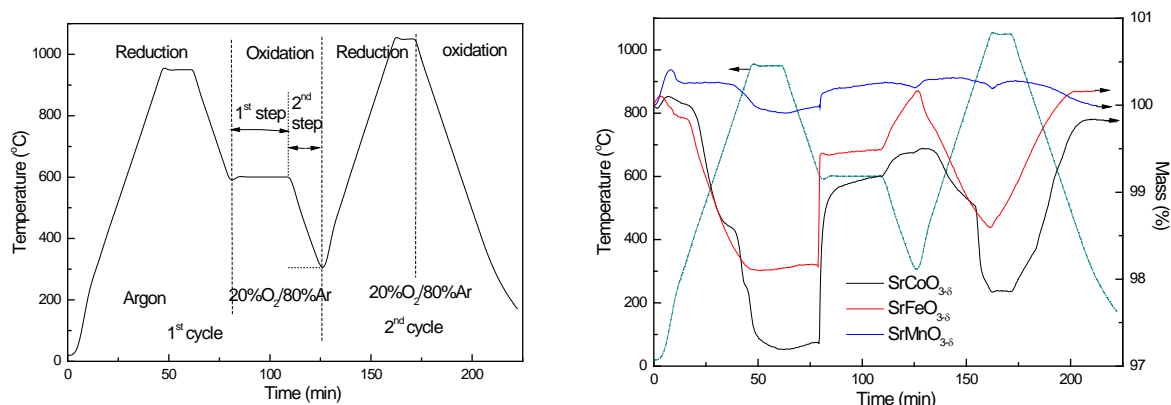


Figure 11 TGA heating and operating conditions (left) used for the analyses and the redox behaviour of $\text{SrBO}_{3-\delta}$ (B=Fe, Co and Mn) perovskites (right).

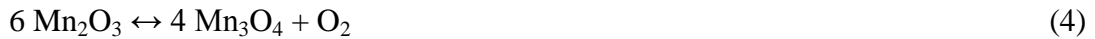
The O_2 exchange of Co-based perovskites is rapid, and it seems that there is a transition in the oxidation state when reaching a given temperature. In contrast, the O_2 exchange rate of Fe-based perovskites is corresponding to the temperature variation, which points out the fast kinetics as the equilibrium state is reached for each temperature of the non-isothermal profile. Finally, the Mn-based systems are almost unchanged during the course of the redox cycles in the considered temperature range, which denotes their high stability and unsuitability for thermochemical redox cycling under the given reaction conditions (Table 3).

Table 3 O_2 exchange capacity and difference in non-stoichiometry of different perovskite samples (mol oxygen per mol perovskites).

Samples	1 st cycle			2 nd cycle	
	Red.	1 st step oxid. (600°C)	2 nd step oxid.	Reduction	Oxidation
$\text{SrMnO}_{3-\delta}$	0.06	0.03	0	-	-
$\text{SrCoO}_{3-\delta}$	0.33	0.21	0.03	0.18	0.17
$\text{SrFeO}_{3-\delta}$	0.24	0.16	0.08	0.19	0.18
$\text{BaMnO}_{3-\delta}$	0.11	0	0	-	-
$\text{BaCoO}_{3-\delta}$	0.47	0.49	0.02	0.49	0.37
$\text{BaFeO}_{3-\delta}$	0.45	0.02	0.12	0.14	0.12
SCF-82	0.37	0.14	0.1	0.19	0.19
SCF-28	0.36	0.17	0.1	0.23	0.21
BSC-55	0.45	0.26	0.03	0.29	0.22
BSF-55	0.27	0.12	0.12	0.24	0.24
BSCF-5582	0.23	0.11	0.1	0.18	0.2
BSCF-5528	0.26	0.15	0.09	0.19	0.2

4. Integration of Thermochemical Storage Systems: A Case Study¹ (PSI)

This case study investigates how the gas-solid contacting pattern in a thermochemical storage (TCS) system influences (1) the integration of the storage into a concentrated solar power (CSP) plant and (2) the resulting performance of the CSP plant. The manganese oxide redox-cycle



is chosen as the model reaction system. The TCS system is operated with air acting as both heat transfer fluid (HTF) and carrier of the gaseous reactant/product (O_2).

As TCS essentially presents a gas-solid chemical reactor operating in an unsteady-state regime, the proper selection and design of a specific TCS configuration should stem from the principles that have been well established by reaction-engineering practice [21]-[22]. According to those principles, the particle size distribution of the TCS material affects not only the gas-solid reaction kinetics but it also imposes a specific reactor type. Sub-millimetre particles with a broad size distribution are generally handled in fluidized-bed reactors because packed beds comprising such particles suffer from excessive gas channelling induced by large pressure gradients. Conversely, larger, uniformly-sized granules or pellets (>2 mm) are generally suitable for packed-bed reactors as fluidized beds tend to spout for such granules or pellets, which is undesirable for physical and chemical operations [22].

The two reactor types, fluidized and packed beds, feature different contacting patterns that, in turn, lead to different spatial and temporal temperature distributions of gas and solids. Namely, due to good mixing the temperature of the solids in a fluidized bed can be considered spatially uniform so that the gas leaves the bed at the temperature of the solids [22]. On the contrary, in a packed bed, the solids do not mix and thus their temperature varies with both time and space. The difference in the spatial temperature distributions of the solid phase in these two reactor types is reflected by the difference in the temporal outflow temperatures of the HTF, which ultimately influences the integration of the TCS into the CSP plant.

To determine the role of the reactor type in imposing the optimal TCS integration into a CSP plant, the reactors are modelled based on empirical reduction/oxidation rate laws that are adjusted for the intra-particle diffusion in the granules. Two idealized contacting patterns are assumed: (1) an axially-dispersed plug flow of gas through stationary solids for the packed bed and (2) a plug flow of gas through a well-mixed batch of solids for the fluidized bed, such that the gas leaves the bed at the temperature of the solids. The solids are assumed to have a diameter of 5 mm in the packed bed and 100 μm in the fluidized bed, respectively.

¹ Material presented in this section has been published in [25].

Figure 12 shows a comparison of the air temperatures as a function of time at the inlet and outlet of the packed and fluidized beds operated under quasi-steady-state conditions². For both reactor types, air enters the bed at $T_{f,c,in} = 1273$ K during a charging period of 6 hours and at $T_{f,d,in} = 373$ K during a discharging period of 6 hours (see solid lines). The packed bed TCS is charged by feeding hot air from the top and discharged by feeding cold air from the bottom. Because of this flow reversal, the axial temperature gradient in the solid phase can be maintained throughout the entire charging-discharging cycle, and thus the granules at the bottom are not heated appreciably. Therefore, the HTF leaves the packed bed at a constant temperature of $T_{f,c,out} = 373$ K during the entire charging period (dashed line). Different from the packed bed, the temperature of the solids in the fluidized bed is uniform due to spatial mixing. Since the HTF approaches the temperature of the solids, the HTF outflow temperatures during charging and discharging are coupled to the temperatures at which the reduction and oxidation are favourable, respectively. Therefore, the HTF leaves the fluidized bed at $T_{f,c,out} \approx 1180$ K during most of the charging period and at $T_{f,d,out} \approx 1090$ K during most of the discharging period. Whereas the HTF outflow temperatures of the two reactor types are similar during discharging, it is important to note that during charging the outflow temperature of the fluidized bed is significantly higher.

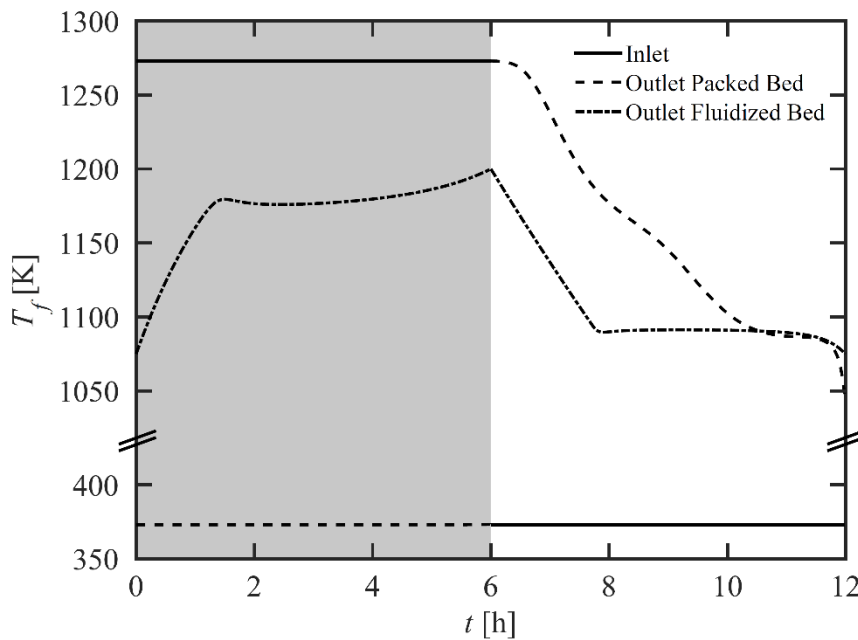


Figure 12 Comparison of air temperatures as a function of time at the inlet of the packed and fluidized beds (solid lines), the outlet of the packed bed (dashed line), and the outlet of the fluidized bed (dash-dotted line) during a charging-discharging cycle.

² Quasi-steady state was considered reached when the maximum local temperature difference between the final states of two subsequent cycles was less than 0.01 K in the gas phase.

The preferred integration of the TCS into the CSP plant is selected based on the computed HTF outflow temperatures and the requirements by both the power block and the solar field. The first and common way of storage integration is the parallel configuration shown in Figure 13, in which the mass flow leaving the solar field is split into a portion flowing through the storage heat exchanger (HX) and the remainder flowing through the power-block HX. The second option is the serial configuration shown in Figure 14, where the entire flow of the HTF leaving the solar field is passing first through the storage and then through the power-block HXs. The parallel and serial configurations must satisfy several constraints for efficient operation. During discharging, the constraints are identical: the storage should provide heat at temperatures that are sufficiently high to run the power block. For this case study, it is assumed that this constraint is fulfilled. During charging, however, the constraints are not identical. In the serial configuration, $T_{f,c,out}$ must be high enough to drive the power block. The parallel configuration requires $T_{f,c,out} \approx T_{PB,out}$ to reduce exergy losses due to mixing. These constraints, and the results presented above on the air outflow temperatures during charging, can now be seen to dictate how packed and fluidized bed reactors should be integrated into a CSP plant.

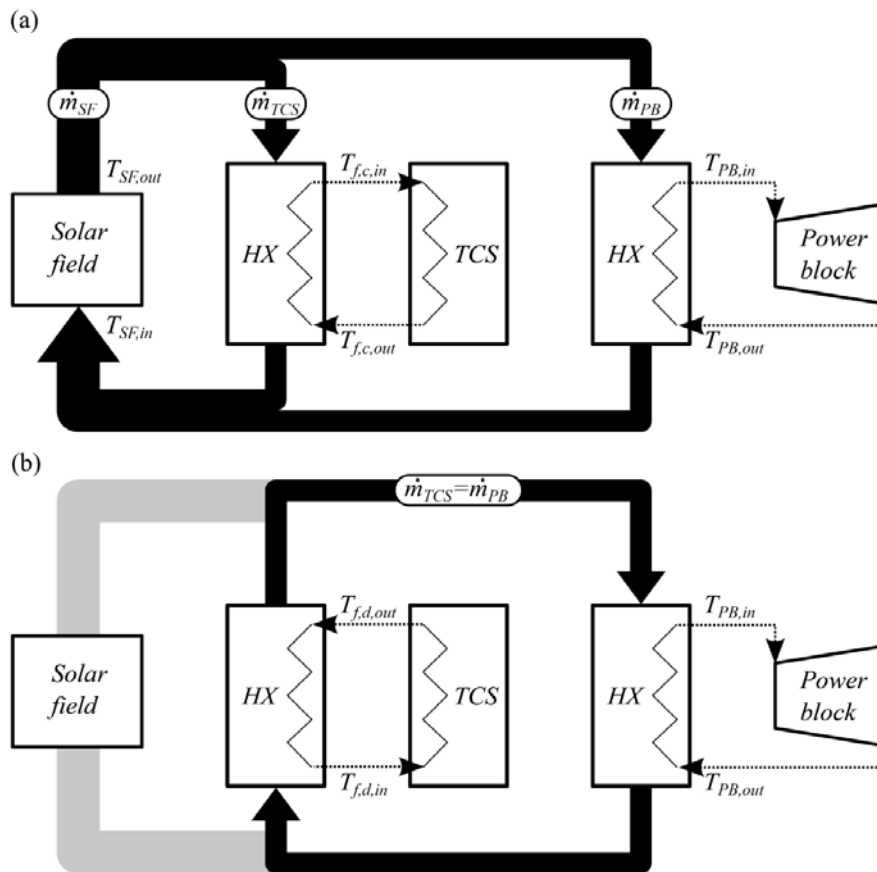


Figure 13 Schematic depiction of a parallel configuration of the TCS and the power block during (a) charging and (b) discharging.

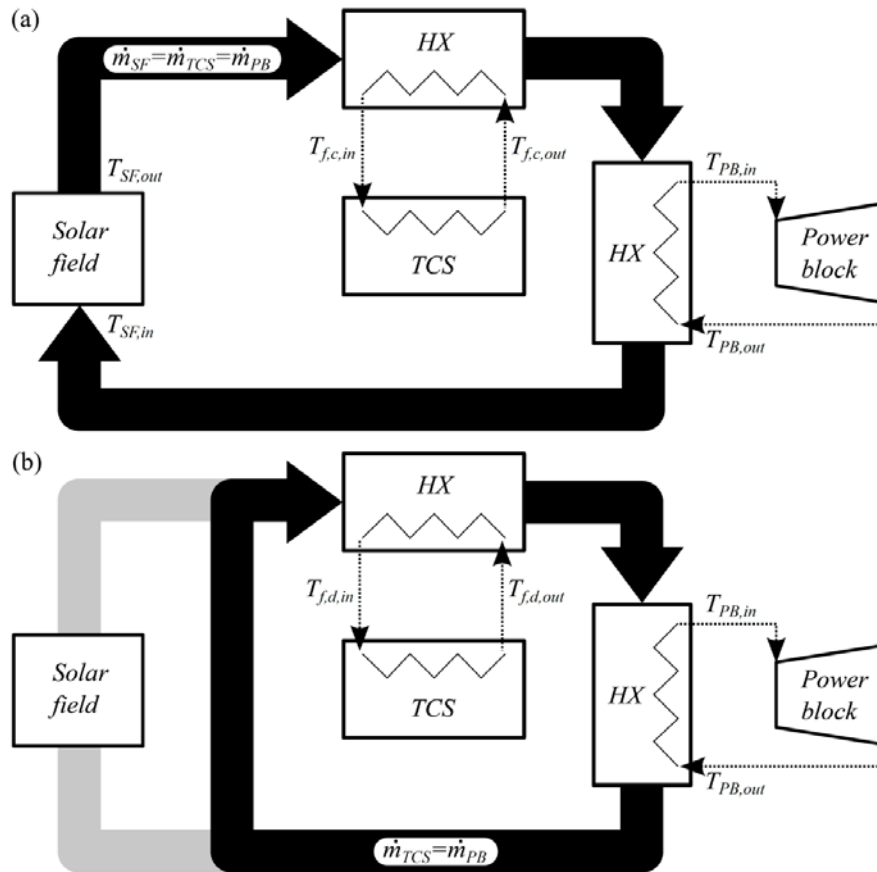


Figure 14 Schematic depiction of a serial configuration of the TCS and the power block during (a) charging and (b) discharging.

For a packed bed TCS, the chosen operating conditions allow for $T_{f,c,out} \approx T_{f,d,in} = T_{PB,out}$, thus the streams from the TCS and power-block HXs can be merged with low exergy losses. Accordingly, a parallel configuration is chosen for the packed bed. Conversely, for a fluidized bed, $T_{f,c,out}$ is coupled to the reduction temperature T_{red} and therefore $T_{f,c,out} \approx T_{red} \gg T_{PB,out}$. A parallel configuration would therefore lead to large exergy losses due to mixing. Accordingly, a serial configuration is chosen for the fluidized bed.

Having determined suitable CSP plant configurations for packed and fluidized bed TCS reactors, these configurations will now be assessed using the following criteria: (1) gravimetric energy storage density, (2) HTF temperature at the power-block inlet, and (3) flexibility in adjusting the electricity production.

The gravimetric energy storage density \bar{e}_{tot} relates the energy that can be stored in a TCS reactor during one charging period to the mass of storage material in the bed. The higher \bar{e}_{tot} , the less material is required to reach a given storage capacity and the lower the storage material costs. \bar{e}_{tot} is given by the sum of the chemically stored energy e_{chem} , which is calculated from the change in solid conversion between the beginning and the end of charging, and the sensible heat e_{sens} , which is calculated from the temperature increase the solids are subjected to during the charging period. The resulting contributions of sensible and chemically stored energy in the packed and fluidized beds are compared in Table 4. It is seen

that about 63% of the total energy is stored chemically in the fluidized bed. By contrast, the chemically stored energy accounts for only about 9% of the total stored energy in the packed bed because only about 14% of the storage material has reacted. Nevertheless, the gravimetric energy storage density of the packed bed is approximately 11% higher than that of the fluidized bed because of the much larger proportion of sensible heat. Thus, it is important to account for the contribution of the sensible heat when comparing TCS reactor types. It should be emphasized that these results are valid only for this specific case study because they are dependent on the reaction system and the operating conditions.

Table 4 Contribution of sensible (e_{sens}) and chemically stored energy (e_{chem}) to the gravimetric energy storage densities (\bar{e}_{tot}) in the packed and fluidized beds.

	e_{sens} [MJ/kg _{Mn₂O₃}]	e_{chem} [MJ/kg _{Mn₂O₃}]	\bar{e}_{tot} [MJ/kg _{Mn₂O₃}]
Packed bed	0.304 (91%)	0.030 (9%)	0.334
Fluidized bed	0.111 (37%)	0.189 (63%)	0.300

As long as the maximum operating temperature of the power block is not exceeded, higher temperatures at the inlet of the power block are desirable. They may offer at least one of the following advantages: (1) more compact HX that couples the HTF from the solar field with the working fluid of the power block; (2) potential increase of heat-to-electricity conversion efficiency of a given power cycle according to Carnot's principle; and/or (3) application of a different power block technology that operates at higher temperatures and, thereby, with increased efficiencies (e.g., Rankine cycle combined with gas turbine) [23]-[24]. In the parallel configuration, thermal energy is transferred directly from the solar field to the power block during charging (see Figure 13a), and therefore $T_{PB,in} = T_{SF,out} = 1273$ K. Conversely, in a serial configuration, some of the thermal energy is transferred to the TCS before entering the power block (see Figure 14a), and therefore $T_{PB,in} = T_{f,c,out} < T_{f,c,in} = T_{SF,out}$ (see dash-dotted line for charging in Figure 12). Thus, $T_{PB,in}$ is generally higher during charging for a parallel configuration than for a serial configuration. Note that in this study, the packed bed in a parallel configuration also leads to higher values of $T_{PB,in}$ during most of the discharging phase as can be seen from the outflow temperatures during discharging in Figure 12.

The flexibility in adjusting the electricity production in the parallel and serial configurations has been compared in detail in [25]. For the sake of brevity, only the most important difference between the two configurations is presented here. By appropriate sizing of the solar field and adjustment of the HTF mass flow rates in a parallel configuration, the charging rate of the TCS ($\dot{Q}_{TCS,c}$) can be set independently of the rate at which heat is transferred to the power block ($\dot{Q}_{PB,c}$). Thus, it can be ensured that sufficient heat is transferred to the TCS during charging to reach the desired duration τ_d of subsequent discharging. Conversely, in a serial configuration, the HTF transfers heat to the TCS before entering the power block. Therefore, if $T_{SF,out}$ and $T_{PB,out}$ are given by the corresponding CSP plant components, $T_{f,c,out}$ becomes the only parameter that allows the relative TCS charging rate $\dot{Q}_{TCS,c} / \dot{Q}_{PB,c}$ and thus the attainable τ_d to be adjusted. This generally leads to a trade-off in serial configurations. A decrease in $T_{f,c,out}$, achieved via variation of the reactor type, operating conditions, and/or the reaction system, leads to an increase in the attainable duration of discharging; however, it also reduces $T_{PB,in}$, thereby potentially lowering the thermal-to-electricity efficiency of the power

block. A parallel configuration is not subject to this trade-off.

Based on these assessment criteria, it can be concluded that a TCS reactor should be designed such that it can be integrated with the power block in a parallel configuration. As mentioned earlier, in a parallel configuration $T_{f,c,out}$ should be kept close to $T_{PB,out}$ to minimize exergy losses. Since the reduction usually takes place at temperatures that are significantly higher than $T_{PB,out}$, the high-temperature reaction zone should be combined with a cooling zone, in which the HTF is cooled from the reduction temperature down to $T_{f,c,out} \approx T_{PB,out}$. Although the presented packed bed TCS is suitable for a parallel configuration, it converts only a fraction of the reactants (~14%). The non-reacting portion of the reactants could thus be replaced by low-cost inert materials, leading to a combined thermochemical-sensible energy storage consisting of a high-temperature reaction TCS zone and a sensible-heat storage unit as the cooling section. Further reactor concepts that would also fulfil the requirements for integration into a parallel configuration are discussed in [25].

5. List of abbreviations

CNRS	Centre National de la Recherche Scientifique, France
CSP	Concentrating Solar Power
IMDEA	Instituto Madrileño de Estudios Avanzados, Móstoles, Spain
HRSEM	High-Resolution Scanning Electron Microscopy
HTF	Heat Transfer Fluid
HX	Heat Exchanger
PSI	Paul Scherrer Institute, Switzerland
SEM	Scanning Electron Microscopy
TCS	Thermochemical Storage
TES	Thermal Energy Storage
TGA	Thermogravimetric Analysis
XRD	X-Ray Diffraction

6. References

- [1] A.H. Abedin, M.A. Rosen. A critical review of thermochemical energy storage systems. *The Open Renewable Energy Journal*, 2011, 4, 42-46.
- [2] A. Solé, X. Fontanet, C. Barreneche, I. Martorell, A.I. Fernández, L.F. Cabeza. Parameters to take into account when developing a new thermochemical energy storage system, *Energy Procedia*, 2012, 30, 380-387.
- [3] A. Solé, I. Martorell, L.F. Cabeza. State of the art on gas-solid thermochemical energy storage systems and reactors for building applications, *Renew. Sustain. Energy Reviews*, 2015, 47, 386-398.
- [4] B. Wong, L. Brown, F. Schaube, R. Tamme, C. Sattler. Oxide based thermochemical heat storage. Presented at SolarPACES, 2010, Perpignan, France.
- [5] M. Neises, S. Tescari, L. De Oliveira, M. Roeb, C. Sattler, B. Wong, Solar-heated rotary kiln for thermochemical energy storage. *Solar Energy*, 2012, 86, 3040-3048.
- [6] C. Agrafiotis, M. Roeb, M. Schmücker, C. Sattler. Exploitation of thermochemical cycles based on solid oxide redox systems for thermochemical storage of solar heat. Part 2: Redox oxide-coated porous ceramic structures as integrated thermochemical reactors/heat exchangers. *Solar Energy*, 2015, 114, 440-458.
- [7] C. Agrafiotis, S. Tescari, M. Roeb, M. Schmücker, C. Sattler. Exploitation of thermochemical cycles based on solid oxide redox systems for thermochemical storage of solar heat. Part 3: Cobalt oxide monolithic porous structures as integrated thermochemical reactors/heat exchanger. *Solar Energy*, 2015, 114, 459-475.
- [8] G. Karagiannakis, C. Pagkoura, A. Zygogianni, S. Lorentzou, A.G. Konstandopoulos. Monolithic ceramic redox materials for thermochemical heat storage applications in CSP plants. *Energy Procedia*, 2014, 49, 820-829.
- [9] T. Block, N. Knoblauch, M. Schmücker. The cobalt-oxide/iron-oxide binary system for use as high temperature thermochemical energy storage material. *Thermochimica Acta*, 2014, 577, 25-32.
- [10] A.J. Carillo, D.P. Serrano, P. Pizzaro, J.M. Coronado. Thermochemical heat storage based on the Mn_2O_3/Mn_3O_4 redox couple: influence of the initial particle size on the morphological evolution and cyclability. *J Mater Chem A*, 2014, 2, 19435-19443.
- [11] A.J. Carillo, D.P. Serrano, P. Pizzaro, J.M. Coronado. Improving the Thermochemical Energy Storage performance of the Mn_2O_3/Mn_3O_4 redox couple by the incorporation of iron. *ChemSusChem*, 2015, 8, 1947-1954.
- [12] A.J. Carillo, D.P. Serrano, P. Pizzaro, J.M. Coronado. Manganese oxide-based thermochemical energy storage: Modulating temperatures of redox cycles by Fe-Cu co-doping. *J. Energy Storage*, 2016, 5, 169–176. DOI:[10.1016/j.est.2015.12.005](https://doi.org/10.1016/j.est.2015.12.005)
- [13] K.J. Albrecht, G.S. Jackson, R.J. Braun. Thermodynamically consistent modeling of redox-stable perovskite oxides for thermochemical energy conversion and storage. *Applied Energy* 2016, 165, 285-296.
- [14] T. Masunaga, J. Izumi, N. Miura. Relationship between oxygen sorption properties and crystal structure of Fe-based oxides with double perovskite composition. *Chem Eng Science* 2012, 84, 108-112.

- [15] Q. Shen, Y. Zheng, C. Luo, C. Zheng. Characteristics of $\text{SrCo}_{1-x}\text{Fe}_x\text{O}_{3-\delta}$ perovskite powders with improved O_2/CO_2 production performance for oxyfuel combustion. *Bull Korean Chem Soc* 2014, 35, 6, 1614-1618.
- [16] S.M. Babiniec, E.N. Coker, J.E. Miller, A. Ambrosini. Investigation of $\text{La}_x\text{Sr}_{1-x}\text{Co}_y\text{M}_{1-y}\text{O}_{3-\delta}$ ($\text{M} = \text{Mn, Fe}$) perovskite materials as thermochemical energy storage media. *Solar Energy* 2015, 118, 451-459.
- [17] N. Galinsky, A. Mishra, J. Zhang, F. Li. $\text{Ca}_{1-x}\text{A}_x\text{MnO}_3$ ($\text{A} = \text{Sr and Ba}$) perovskite based oxygen carriers for chemical looping with oxygen uncoupling (CLOU). *Appl Energy* 2015, 157, 358-367.
- [18] S.M. Babiniec, E.N. Coker, J.E. Miller, A. Ambrosini. Doped calcium manganite for advanced high-temperature thermochemical energy storage. *Int. J. Energy Res.*, 2016, 40, 280-284.
- [19] K. Gupta, S. Singh, R.M.S. Rao. Fast, reversible CO_2 capture in nanostructured Brownmillerite $\text{CaFeO}_{2.5}$. *Nano Energy*, 2015, 11, 146-153.
- [20] Z. Zhang, L. Andre, S. Abanades. Experimental assessment of oxygen exchange capacity and thermochemical redox cycle behavior of Ba and Sr series perovskites for solar energy storage. *Solar Energy*, 2016, 134, 494-502.
- [21] G.F. Froment, K. Bischoff, J. De Wilde. *Chemical Reactor Analysis and Design*. Wiley New York. 1990, ISBN: 0-4715-2190-6.
- [22] D. Kunii, O. Levenspiel. *Fluidization Engineering*, Butterworth-Heinemann Boston. 1991, ISBN: 978-0-409-90233-4.
- [23] N.P. Siegel, Thermal energy storage for solar power production. *Wiley Interdiscip. Rev. Energy Environ.* 2012, 1(2), 119–131. DOI: 10.1002/wene.10.
- [24] Z. Ma, G. Glatzmaier, M. Mehos. Fluidized Bed Technology for Concentrating Solar Power With Thermal Energy Storage. *J. Sol. Energy Eng.*, 2014, 136(3), 031014. DOI: 10.1115/1.4027262.
- [25] S. Ströhle, A. Haselbacher, Z.R. Jovanovic, A. Steinfeld. The effect of the gas-solid contacting pattern in a high-temperature thermochemical energy storage on the performance of a concentrated solar power plant. *Energy Environ. Sci.* 2016, 9(4), 1375–1389. DOI: 10.1039/C5EE03204K.